Interplay between metastable phases controls strength and ductility in steels

Hidalgo, J.; Huizenga, R. M.; Findley, K. O.; Santofimia, M. J.

DOI
10.1016/j.msea.2018.12.096

Publication date
2019

Document Version
Final published version

Published in
Materials Science and Engineering A

Materials Science & Engineering A 745 (2019) 185–194

Contents lists available at ScienceDirect

Materials Science & Engineering A

journal homepage: www.elsevier.com/locate/msea

Interplay between metastable phases controls strength and ductility in steels

J. Hidalgo[a,*], R.M. Huizenga[a], K.O. Findley[b], M.J. Santofimia[a]

[a] Department of Materials Science and Engineering, Delft University of Technology, Mekelweg 2, 2628 CD Delft, the Netherlands
[b] G.S. Ansell Department of Metallurgical and Materials Engineering, Colorado School of Mines, Golden, CO, USA

ARTICLE INFO

Keywords:
Multiphase steels
Austenite stability
Martensite strength
Work-hardening
Synchrotron XRD

ABSTRACT

By means of high-energy synchrotron X-ray diffraction, the interplay between martensite and retained austenite phases in steel during the application of stress has been analyzed. Martensite properties were varied through controlled reheating heat treatments in a low carbon Quenched and Partitioned (Q&P) steel consisting of retained austenite and martensite. The reheating treatments significantly altered martensite strength while keeping the same fractions of retained austenite as the non-reheated Q&P microstructures, resulting in different degrees of stress partitioning and work hardening of the individual microconstituents. Results of this study show that the strength ratio between the different phases in the microstructure plays a crucial role in the onset and rate of mechanically induced decomposition of retained austenite. Consequently, the strength ratio between phases controls the yielding and work-hardening of the material.

1. Introduction

Multiphase combinations of metastable austenite embedded in low carbon lath martensite are currently the epitome of optimizing both strength and ductility [1–7] in steels. These materials benefit from mechanically-induced transformation of metastable austenite into martensite, which contributes to increased plastic deformation and simultaneously increases strength [8–10]. Therefore, most studies of microstructural design of multiphase steels focus on designing austenite stability and volume fraction for optimum strength and ductility.

Several factors such as chemical composition, grain size and morphology have been extensively demonstrated to influence the mechanically stability of the retained austenite [5,11–14]. Nevertheless, an increasing number of studies point towards a crucial role of the phases surrounding retained austenite, not only in the mechanical stability of retained austenite, but also in the mechanical response of the material as a whole [15–20]. Thus, Findley et al. [21] identified that martensite strength controls the early stages of work hardening behaviour in austenite/martensite microstructures. Their results also suggested that martensite strength has an important effect on work-hardening at high plastic strains, regulating the work-hardening of individual phases and the retained austenite transformation. However, in these studies the precise contribution of the surrounding martensite in the material work hardening is not fully isolated from other affecting factors.

Recent developments in in-situ high energy synchrotron diffraction (SXRD) and neutron diffraction have enabled to identify the role of different microstructural components on deformation and transformation behaviour of multiphase steels [1,9,22–24]. In the present study, SXRD was employed to continuously monitor the fraction of retained austenite and strain/stress partitioning between retained austenite and martensite during tension testing. The same materials developed in [21], in which martensite with different strength levels was obtained without significantly affecting the other microstructural features, were used in the present this study. This experiment allowed to unravel the effect of martensite strength in the mechanical stability and work-hardening behaviour of austenite/martensite microstructures and to precisely assess the complex interplay between austenite and martensite during the application of uniaxial tensile stress.

2. Experimental methodology

2.1. Materials

The chemical composition of the steel alloy used in this study is provided in Table 1. The steel was produced using a laboratory vacuum induction furnace. After casting, the steel was hot rolled to a final thickness of 4 mm and then air cooled. Three different thermal cycles, detailed in Fig. 1a, were selected according to previous works [21,25]. They are labeled as LT, MT and HT referring to low, medium and high degree of tempering of the martensite in the microstructure, respectively. LT is a conventional quenching and partitioning heat treatment

* Corresponding author.
E-mail address: J.HidalgoGarcia@tudelft.nl (J. Hidalgo).

https://doi.org/10.1016/j.msea.2018.12.096
Received 10 September 2018; Received in revised form 7 December 2018; Accepted 20 December 2018
Available online 21 December 2018

Table 1
Composition, in wt%, of the steel alloy used in the study.

C	Mn	Si	Mo	Al	S	P	Fe
0.20	3.51	1.525	0.509	0.03	0.0079	0.006	Balance

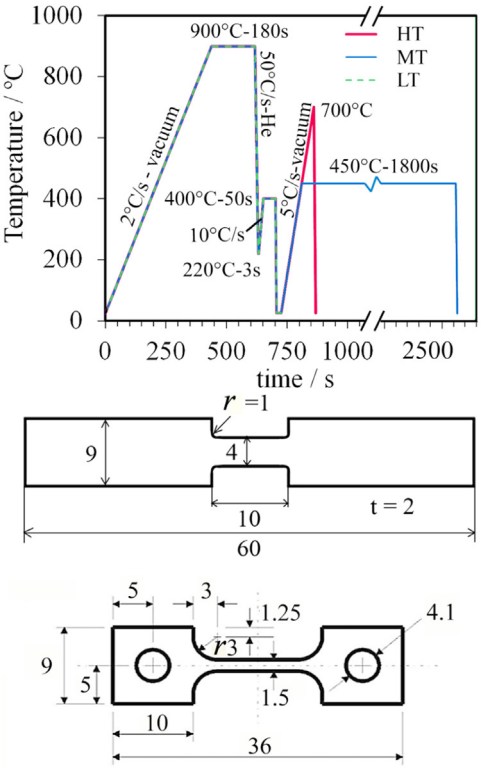

Fig. 1. (a) Thermal history of different materials used in this study. (b) Drawing of the specimen dimensions heated at dilatometer and (c) tensile specimen geometry used in the in-situ SXRD experiments.

(Q&P), leading to an austenite/martensite microstructure in which primary martensite formed during the first cooling step is weakly tempered during a subsequent partitioning step at 400 °C for 50 s. MT and HT are reheating treatments to different temperatures from the LT baseline treatment with the objective of further tempering the martensite to greater extents. Fig. 7a schematizes three different fine-grained austenite/martensite microstructures specifically created by application of the tailor-made heat treatments. This scheme is based on previous microstructure characterization that can be found elsewhere in [24]. Metastable austenite films are embedded in a lath martensitic matrix. All microstructures have approximately equivalent fraction, size and morphology of the different microconstituents and austenite chemical composition as shown in Table 2. The only significant difference is the degree of tempering of martensite resulting in different martensite strength due to differences in carbon content, carbide fraction and dislocation density. To schematically highlight the degree of martensite tempering, the parameter carbon content multiplied by dislocation density is created and coded in grey scale in Fig. 7a.

2.2. Sample preparation

Specimens with the geometry shown in Fig. 1b were machined for dilatometry heat treatments parallel to the rolling direction (RD) of the sheet material. Accurate temperature-controlled heat treatments were performed with a Bähr 805 DIL A/D dilatometer. A type S thermocouple spot-welded on the surface was used to monitor temperature. A vacuum on the order of 10^{-4} mbar was used during heating or isothermal segments, and helium was used as the cooling gas.

After heat treatments, flat tensile specimens were extracted from the previous geometry as shown in Fig. 1c. These specimens had a gauge length of 10 mm and a square cross-section of 1.5 mm of width and thickness. Specimen surfaces were ground to 2000 grit silicon carbide sand paper.

2.3. High-energy synchrotron x-ray diffraction experiment

The in-situ SXRD experiments were performed at the ID11 beam line of the European Synchrotron Radiation Facility (Grenoble, France). A monochromatic X-ray beam of wavelength of $\lambda = 0.15582$ Å and a beam size of $400 \times 400\ \mu m^2$ illuminated the sample in transmission geometry as schematized in Fig. 2a. The large amount of analyzed material enabled a statistical representation of the microstructure to be analyzed. The diffracted beam was recorded onto a two dimensional (2D) CCD detector (FRELON) placed 301.7 mm behind the sample. This configuration allowed the characteristic diffraction rings of the {*hkl*} planes of the face centered cubic (fcc) austenite (γ) and body centered cubic (bcc) martensite (α') phases to be captured as indicated in Fig. 2b. The relevant instrumental parameters (specimen-detector distance, coordinates of the beam center and the inclination of the detector with respect to the direct beam) were determined using a CeO_2 calibrant (NIST SRM 674b) placed on the top of the specimen. In addition, Si powder (NIST 640c) was shaped in a specimen with the same dimensions as the gauge of the tensile specimen to determine and correct instrumental broadening.

An Instron/NPL electro-thermal mechanical testing (ETMT) machine was used to study the mechanical response. 2D diffraction patterns were continuously recorded during tensile tests with an exposure time of 0.1 s, having an effective measurement interval of 0.7 s. The fast acquisition rate of the XRD diffractogram during in-situ tensile experiments allowed for precise tracking of austenite fractions and different phase strains at intervals of approximately 4 MPa. The stress was applied along the y-direction, the x-ray beam travels along the x-direction and the z-axis is vertical (Fig. 2b). A load control mode at a constant stress rate of 3.9 MPa/s was used to better track the elastic part and the transition to plastic regime of the strain stress curve. In load control, specimens broke almost immediately after maximum uniform

Table 2
Initial microstructure parameters (unstrained specimen): austenite fraction (f_γ), carbon content (χ_C) and full width half maximum (FWHM) of different phases and crystallographic planes obtained from synchrotron. ρ refers to density of dislocations.

	LT	MT	HT
f_γ	0.14 ± 1	0.14 ± 1	0.12 ± 1
$\chi_{C\gamma}$ (wt%)	0.88 ± 0.02	0.90 ± 0.02	0.90 ± 0.02
$FWHM_{200\gamma}$ (2θ/°)	0.0109 ± 0.0007	0.0081 ± 0.0008	0.0088 ± 0.0010
$FWHM_{220\gamma}$ (2θ/°)	0.0140 ± 0.0007	0.0090 ± 0.0007	0.0111 ± 0.0009
$\chi_{C\alpha'}$ (wt%)	0.11 ± 0.05	0.08 ± 0.05	0.04 ± 0.05
$FWHM_{200\alpha'}$ (2θ/°)	0.0238 ± 0.0003	0.0159 ± 0.0004	0.0072 ± 0.0008
$FWHM_{211\alpha'}$ (2θ/°)	0.0150 ± 0.0006	0.0098 ± 0.0008	0.0045 ± 0.0010
$\rho_{\alpha'}$ (10^{15} m^{-2}) [25]	3.1 ± 0.5	2.1 ± 0.4	0.5 ± 0.2

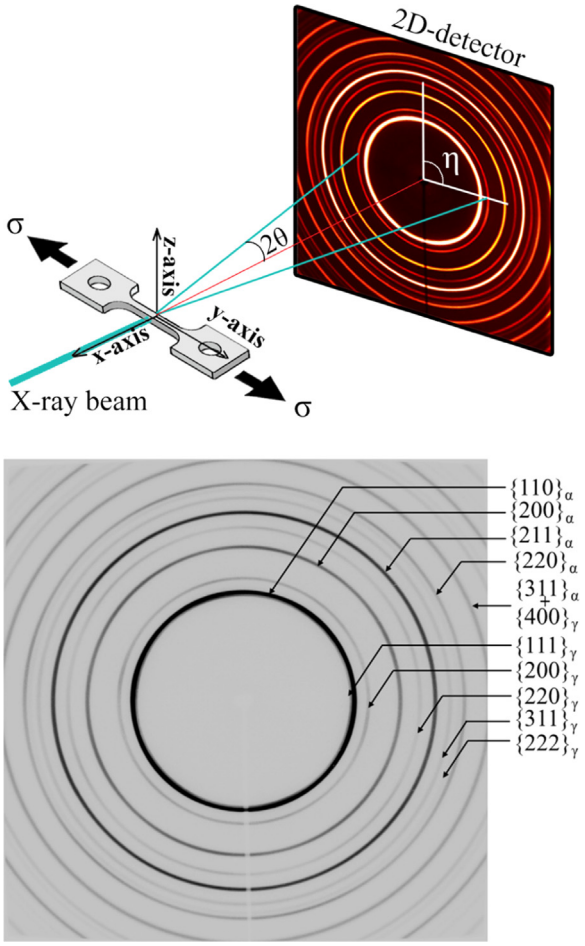

Fig. 2. (a) Schematic of the tensile test where the different axis, loading and X-ray beam direction and relevant angles are indicated. (b) Characteristic 2D-diffraction rings captured in CCD detector, where arrows indicate the phase and the {*hkl*} planes.

elongation was achieved; thus, the development of necking was avoided. The specimen total elongation to failure was determined by correcting crosshead displacement for machine compliance effects.

2.4. Analysis of the diffraction data

The obtained 2D diffraction patterns at different loadings were analyzed using the FIT2D software package [26]. The dark current signal was subtracted and the detector flat field corrected. Afterwards, 2D diffraction patterns were integrated along the scattering angle (2θ) over selected azimuth angles (η), so that one-dimensional diffraction patterns (intensity vs. 2θ) were obtained. Austenite {200}γ and {220}γ and martensite {200}α' and {211}α' reflections, either weakly overlapping or non-overlapping, were fitted to a pseudo-Voigt function after background removal. Then the peak position, the integrated peak intensity and the peak width were determined. Diffraction peaks from stress-induced martensite developed during tensile testing were overlapped with that from primary tempered martensite and small fractions of fresh martensite inherent of the unstrained material. Thus, distinguishing different martensite types was difficult and only the combined peak profile from different martensite were considered to determine the different peak parameters.

2.4.1. Strain and stress evolution in individual {hkl} planes

Individual {*hkl*} plane-strain (ε_{hkl}) can be obtained from the relative change of d_{hkl}:

$$\varepsilon_{hkl} = (d^{\sigma}_{hkl} - d^{0}_{hkl})/d^{0}_{hkl} \tag{1}$$

where d^{σ}_{hkl} and d^{0}_{hkl} correspond to the lattice plane spacing at a given load step and at the unloaded situation, respectively, and are obtained from the Bragg's relation.

Variations in ε_{hkl} with applied stress originate from several contributions, which are separated in this work in two components, the anisotropic (ε^{ani}_{hkl}) and isotropic (ε^{iso}_{hkl}) strains based on Blonde et al. [22,27]:

$$\varepsilon_{hkl} = \varepsilon^{ani}_{hkl} + \varepsilon^{iso}_{hkl} \tag{2}$$

ε^{ani}_{hkl} depends on the lattice plane orientation, and thus has an anisotropic effect. The planes with their normal vector oriented along the loading direction (axial) are in tension, and the planes with their normal vector oriented perpendicular to the loading direction (radial) are in compression. The response of the axial (∥) and radial (⊥) orientations were evaluated by integrating 2D diffraction patterns in azimuth angles (see Figure 2a) $\eta = 0^{\circ} \pm 10^{\circ}$ and $\eta = 90^{\circ} \pm 10^{\circ}$, respectively. The orientation dependence of the strain is defined by the Poisson ratio $= -\varepsilon^{\perp}/\varepsilon^{\parallel}$. For cubic single crystals, the orientation-dependent variation in elastic strain by a tensile stress σ is characterized by the cubic elastic anisotropy factor A_{hkl}:

$$A_{hkl} = \frac{h^2k^2 + l^2k^2 + h^2l^2}{(h^2 + k^2 + l^2)^2} \tag{3}$$

$$\frac{1}{E^{\parallel}_{hkl}} = \frac{\varepsilon^{\parallel}_{hkl}}{\sigma} = S_{11} - 2\left[S_{11} - S_{12} - \frac{1}{2}S_{44}\right]A_{hkl} \tag{4}$$

$$\frac{1}{E^{\perp}_{hkl}} = \frac{\varepsilon^{\perp}_{hkl}}{\sigma} = S_{12} + \left[S_{11} - S_{12} - \frac{1}{2}S_{44}\right]A_{hkl} \tag{5}$$

where E_{hkl} is the elastic modulus of the crystallographic plane and S_{ij} are the elastic compliances. A compilation of material elastic parameters can be found in Table 3. The {200} planes for both austenite and martensite are the most compliant. There was no large difference among all the elastic parameters regardless of phase and heat treatment. Using the Hooke's law, the tensile stress developed in individual crystallographic planes, σ^{11}_{hkl}, can be calculated as follows:

$$\sigma^{11}_{hkl} = \frac{E^{\perp}_{hkl}}{(1+\nu_{hkl})(1-2\nu_{hkl})}\{(1+\nu_{hkl})\varepsilon^{\parallel}_{hkl} + 2\nu_{hkl}\varepsilon^{\perp}_{hkl}\} \tag{6}$$

where $\varepsilon^{\parallel}_{hkl} = \varepsilon_{11}$, $\varepsilon^{\perp}_{hkl} = \varepsilon_{22} = \varepsilon_{33}$.

Interplanar distances, and by extension lattice parameter, are also affected by the interstitial carbon concentration. When austenite mechanically transforms, this transformation takes place preferentially in grains with lower carbon concentration because of lower stability. The higher carbon concentration in the untransformed austenite is reflected in a higher average austenite lattice strain. Moreover, the volume expansion accompanying the austenite to martensite transformation is developed parallel to {220}γ; thus, the newly formed martensite phase

Table 3
Elastic parameters of different crystallographic {*hkl*} planes of austenite and martensite phases in LT, MT and HT specimens: elastic modulus (E), Poisson ratio (ν), elastic compliances (Sij).

	Austenite				Martensite			
	E_{hkl}		ν_{hkl}		E_{hkl}		ν_{hkl}	
	{200}	{220}	{200}	{220}	{200}	{211}	{200}	{211}
LT	162	214	0.39	0.35	154	217	0.32	0.24
MT	154	222	0.31	0.22	160	212	0.32	0.27
HT	158	219	0.37	0.32	158	210	0.31	0.25
	S_{11}	S_{12}	S_{44}		S_{11}	S_{12}	S_{44}	
LT	6.2	− 2.4	11.1		6.5	− 2.1	9.6	
MT	6.5	− 2.0	9.0		6.2	− 2.0	10.5	
HT	6.3	− 2.3	10.3		6.3	− 2.0	10.3	

inside the parent austenite grain compresses the untransformed residual austenite [24]. All the aforementioned effects will have an isotropic effect on strain, i.e. will be independent of plane orientation with respect to the load. ε_{hkl}^{iso} can be calculated by [22,27]:

$$\varepsilon_{hkl}^{iso} = [\varepsilon_{hkl}^{\perp} + \nu\varepsilon_{hkl}^{\parallel}]/(1+\nu) \quad (7)$$

2.4.2. Austenite phase fractions

The evolution of the integrated intensity of the different {*hkl*} reflections provides information about changes in phase fractions and/or texture due to grain rotation into preferential directions or preferential mechanical transformation of austenite grains oriented in particular directions. Neglecting the presence of carbides and considering that only martensite and austenite phases are present in the microstructure ($f_{\alpha'} + f_{\gamma} = 1$), the volume fraction of austenite (f_{γ}) is obtained from the ratio of measured integrated intensities (I) of austenite and martensite peaks to the R-value [28]:

$$f_{\gamma} = \frac{\frac{1}{n}\sum_{l=1}^{n}\frac{I_l^{\gamma}}{R_l^{\gamma}}}{\frac{1}{n}\sum_{l=1}^{n}\frac{I_l^{\gamma}}{R_l^{\gamma}} + \frac{1}{m}\sum_{l=1}^{m}\frac{I_l^{\alpha'}}{R_l^{\alpha'}}} \quad (8)$$

The parameter, R, depends upon interplanar spacing (d_{hkl}), the Bragg angle, θ, crystal structure, and composition of the phase being measured and is calculated from basic principles [29]. It is assumed that the austenite fraction value is not affected by the presence of mechanically induced martensite, because the sum of the structure factors of overlapped individual martensite peaks is practically identical to that of the combined martensite peak. The integrated intensities of individual reflections were obtained from the integration of the diffraction ring over all azimuth angles to avoid texture effects expected during the application of stress.

2.4.3. Average carbon content in austenite

The carbon concentration within austenite during strain application, χ_C, was determined from its lattice parameter a_{γ}, (in Å) as [29]:

$$a_{\gamma} = 3.556 + 0.0453\chi_C + 0.00095\chi_{Mn} + 0.0056\chi_{Al} \quad (9)$$

where χ_i, in wt%, represents the concentration of the alloying element *i*. a_{γ} is calculated from the equation [22]:

$$a_{\gamma} = a_{0\gamma}(1+\varepsilon^{ISO}) \quad (10)$$

where $a_{0\gamma}$ is the austenite lattice parameter before the application of strain and is determined from the {200}γ peak position, $d_{0\{hkl\}}$, with the formula for cubic crystals:

$$a_{\gamma 0} = d_{0\{hkl\}}\sqrt{h^2 + k^2 + l^2} \quad (11)$$

The austenite lattice is compressed preferentially in the direction normal to {220}γ [24,30] due to the volume expansion of the freshly formed martensite within austenite, which explains the shift to compressive strain in the isotropic strain of {220}γ planes in Fig. 3. The carbon concentration in austenite was therefore estimated only by considering the isotropic strain of {200}γ and assuming the isotropic strain is mainly affected by an increase of carbon concentration in solid solution in this particular plane, whereas the effect of lattice compression due to new martensite formation was considered negligible in this plane [30].

2.4.4. Identification of phase yielding

X-ray diffraction captures only elastic deformation through the change in the distance between lattice planes. The occurrence of plastic behaviour and thus the yielding of different phases, however, can be still identified in several ways with SXRD:

1. Peak broadening: It is widely accepted that plastic deformation is accompanied by massive multiplication of dislocations acting as Frank-Read sources and consequently by significant changes in the dislocation structure and density. Crystal lattice distortions, mainly caused by dislocations, determine the diffraction peak width. Therefore, the occurrence of plastic deformation can be resolved by the observation of diffraction peak broadening. Fig. 4 shows the peak broadening evolution of different martensite and austenite peaks as a function of applied stress. At low applied stress, negligible peak broadening is observed, but peak broadening becomes obvious near the yield stress or as austenite destabilizes and starts transforming. Two factors should be considered in the application of this method to the present materials: 1) Peak broadening of austenite can be influenced by a reduction of grain size (diffraction domain) as retained austenite transforms, 2) Mechanically induced martensite has a high carbon concentration in solid solution and dislocation density compared to that of the primary tempered martensite, affecting the peak broadening. Both factors are not expected to have a large influence on the peak broadening until a considerable amount of retained austenite to martensite transformation occurs. Still, austenite transformation into martensite may occur before the yielding of any of the phases.
2. Peak intensity: when texture is evolved with plastic deformation, the fraction of grains oriented in a particular direction may vary, which is reflected in the intensity of the peaks. As an example, the intensity of {200}α' planes oriented parallel to the load direction with stress, depicted in Fig. 5, decreases at a certain stress indicating yielding. A similar trend is observed in {211}α'. In the case of austenite peaks in all specimens, the observed decrease of peak intensity cannot be directly related to grain rotation, and thus yielding, because it is mainly associated with mechanically-induced transformation of austenite into martensite.
3. Stress/strain partitioning: Austenite/martensite microstructures behave as a composite material with the martensite acting as the matrix phase. At the onset of plastic flow of the soft phase, the tangent modulus of the soft phase decreases, offering less resistance to deformation. A relaxation of plane stress deviating from linear behaviour indicates that a phase is yielding. Additional plastic deformation induces a plastic misfit which must be accommodated by an increased elastic strain in the hard phase to satisfy the deformation compatibility. As a result, the stress will be transferred more rapidly to the hard phase, and stress partitioning occurs between different phases.

Peaks broadening, peaks intensity and stress/strain partitioning are analyzed together to identify yielding of individual phases. Moreover, to support the experimental identification, the yield stress of austenite is theoretically estimated in this work from the empirical equation adapted from [31]:

$$\sigma_{ss}^{\gamma} = 15.4\left(4.4 + 23\chi_C + 1.3\chi_{Si} + 0.94\chi_{Mo} + \frac{0.46}{\sqrt{d_{\gamma}}}\right) \quad (12)$$

where χ_j and d_{γ} are the concentration (wt%) of element j (j = C, Si, Mo) in retained austenite and the grain size of retained austenite respectively. To have an idea of the magnitude order of the yield strength in present materials, Eq. (12) is used considering that the content of substitutional elements in the austenite is similar to the nominal composition of the steel, the carbon content is 0.88 wt% and the grain size is 200 nm. Under these assumptions, the yield stress of retained austenite is estimated to be 920 MPa.

3. Results and discussion

3.1. Measurements in unstrained specimens

SXRD measurements in unstrained specimens enabled to determine initial microstructure parameters, which are shown in Table 2. Initial

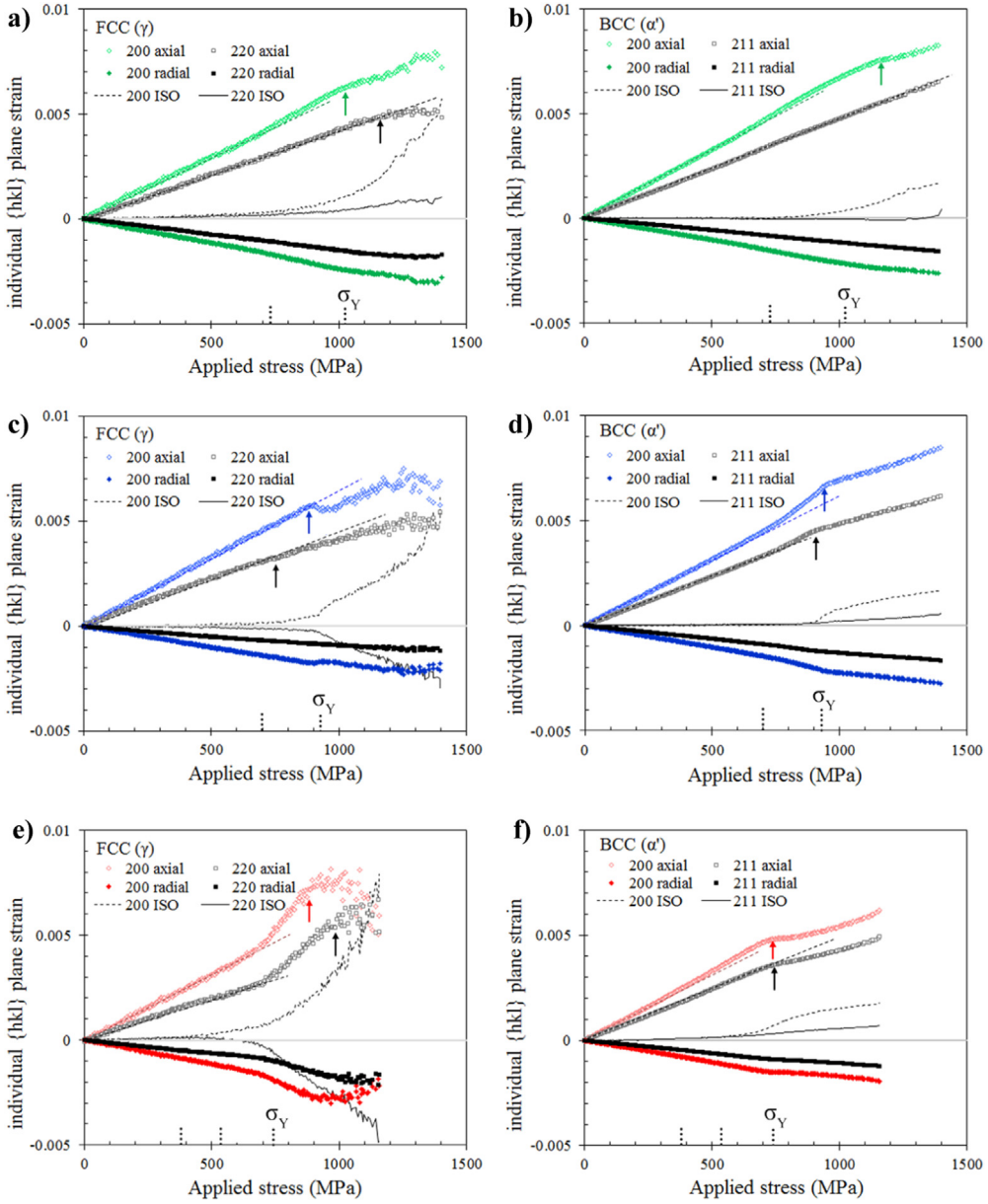

Fig. 3. Evolution of isotropic (ISO) and anisotropic plane strain as a function of applied stress of {200}γ and {220}γ, (a) LT, (c) MT and (e) HT specimens, and {200}α' and {211}α' in (b) LT, (d) MT and (f) HT. The arrows indicate yielding of grains with specific {200} and {211} planes oriented parallel to the load direction. Dashed supplementary lines indicate the linear elastic behaviour. The dotted lines close to the x-axis denote the anelastic region of the material and the yield stress, $\sigma_{Y,}$ of the material.

austenite fraction is similar in the three specimens. As mentioned in Section 2.3, lattice parameter is calculated from {200}γ reflection as it is mainly affected by the composition of austenite. Table 2 shows that the average carbon content in austenite is equivalent in LT, MT and HT specimens as calculated from Eq. (9). The carbon concentration in martensite, $\chi_{C\alpha'}$, is calculated based on its lattice parameter, $a_{\alpha'}$ according to [32]:

$$\chi_{\alpha,} = 31\ \text{wt\%/Å}(a_{\alpha,} - a_{\alpha}) \tag{13}$$

where $a_{\alpha} = 2.866\text{Å}$ is the lattice parameter of a reference sample [33]. A reduction of carbon content in martensite is observed from LT to HT in Table 2, which is in accordance with an increase of fraction and size of carbides as detailed in [21,25]. Table 2 also indicates that the width of the {200}α' and {211}α' peaks in the unloaded condition narrows 35 ± 1% from LT to MT and 70 ± 1% from LT to HT. The decrease in martensite peak broadening is indicative of reduction of lattice distortion in martensite and is congruent with the decrease in martensite dislocation density measured with one dimension XRD and EBSD in [21]. Table 2 shows that {200}γ and {220}γ austenite peaks narrow around 30 ± 2% from LT to MT and 20 ± 4% from LT to HT. The analysis of austenite and martensite peaks in one dimension XRD measurements in [21,25] indicates a weak decrease of austenite peak width in the unloaded condition as the severity of tempering increases (20% from LT to HT on average) compared to a more obvious reduction of peak width in martensite (60% from LT to HT on average), which is in agreement with current observations. In the present steel microstructures, it is reasonable to assume that strains are introduced in austenite by the formation of martensite and due to the mismatch between austenite and martensite thermal expansion during heating and cooling process [30,34]. These compressive hydrostatic strains, which are believed to favour the stability of austenite [34], might not have a large influence in the dislocation density of austenite but affect the peak

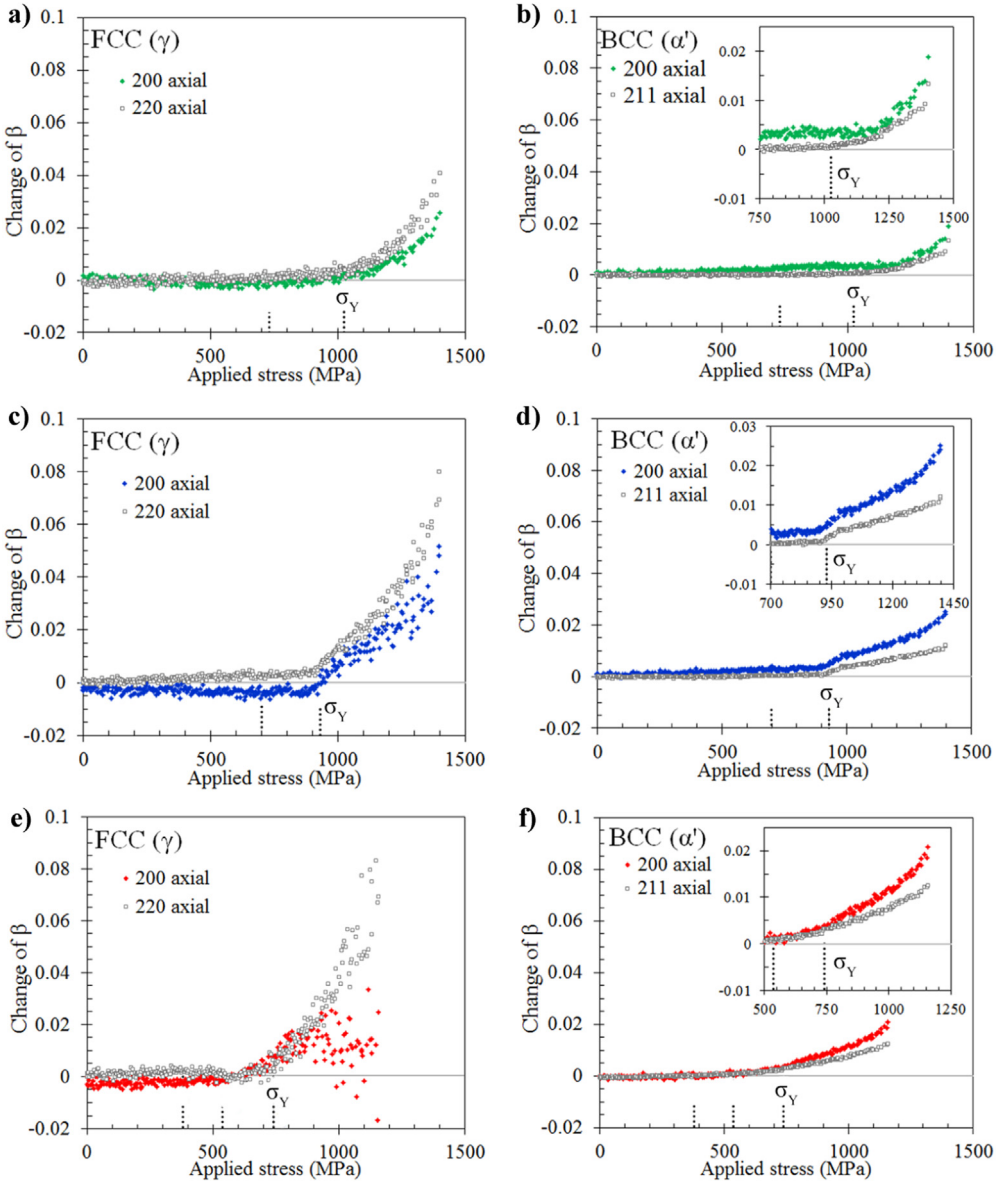

Fig. 4. Peak broadening evolution with applied stress of {200}γ and {220}γ, (a) LT, (c) MT and (e) HT specimens, and {200}α' and {211}α' in (b) LT, (d) MT and (f) HT. The dotted lines close to the axis delimit the anelastic region of the material and σ_Y the yielding of the material.

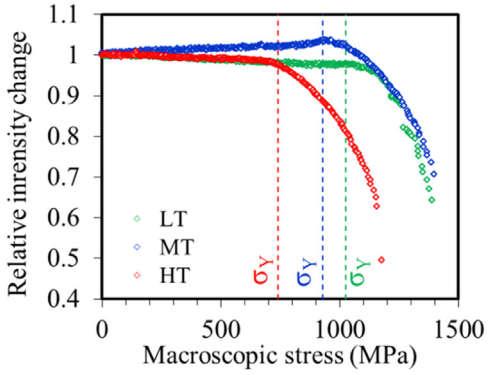

Fig. 5. Relative peak intensity of {200}α' as a function of applied stress of LT, MT and HT specimens. Dashed lines indicate yielding of the material, σ_Y.

broadening. Moreover, these strains are likely partially recovered during tempering or reheating. Therefore, comparing the peak width of austenite and martensite of the different specimens in the unstrained condition, it is assumed that there is a small decrease of dislocation density in austenite from LT to HT specimens compared to the reduction of dislocations in martensite. This assumption is in concordance with slow recovery of austenite compared to fast martensite recovery observed by Wang et al. [35].

3.2. Macroscopic mechanical behaviour

Fig. 6a shows the macroscopic true stress-strain (σ-ε) curves of specimens subjected to LT, MT and HT heat treatments. Each data point on the curves represents a X-ray diffraction measurement. Table 4 contains the relevant parameters that characterize tensile behaviour of the different specimens. The flow behaviour and tensile parameters were consistent with Ref [20]. The LT specimen exhibits a yield strength ($\sigma_{y0.2}$) near 1000 MPa, an ultimate tensile strength (UTS) of about 1400 MPa, and a uniform elongation (UE) value of 0.08. The MT exhibits comparable strength levels to the LT condition with a slightly lower yield strength (950 MPa) and similar tensile strength (1400 MPa). The uniform elongation of the MT condition (11%) is slightly higher than the other two conditions. Reheating the LT material to 700 °C (HT

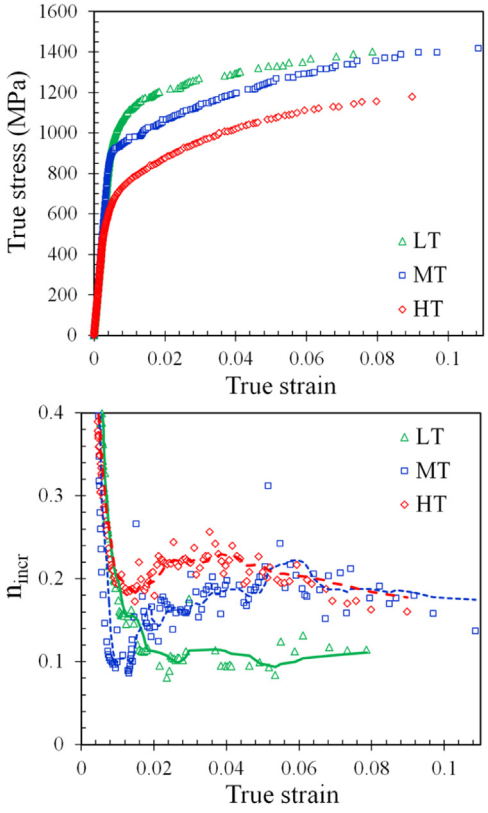

Fig. 6. (a) True stress-strain curves of different materials. (b) Evolution of instantaneous work-hardening rate with true strain.

Table 4
Summary of tensile properties extracted from the strain-strength curves: 0.2% offset yield strength ($\sigma_{Y0.2}$), ultimate tensile strength (UTS), uniform elongation (UE), of the studied materials obtained from the true strain-stress curves. $\sigma y_{0.2}$ is compared with the yield stress obtained from Kocks-Mecking plots, σy_{KM}, according to [37].

	$\sigma_{y0.2}$ (MPa)	σ_{yKM} (MPa)	UTS (MPa)	UE (%)
LT	1039	1025	1402	7.9
MT	918	929	1417	10.9
HT	663	741	1179	9.0

specimen) substantially reduces the yield and the ultimate tensile strength, 650 MPa and 1180 MPa respectively; however, the uniform elongation (9%) is practically unchanged with respect to the LT specimen.

Differences in the work-hardening rate are evident observing the true strain-stress curves of Fig. 6a. For a more detailed analysis, the instantaneous work-hardening rate $n_{incr} = \ln\left(\frac{\sigma_{i+1}}{\sigma_i}\right)/\ln(\varepsilon_{i+1}/\varepsilon_i)$ with strain is shown in Fig. 6b. Both the MT and HT conditions have higher work-hardening rates than the LT condition at true strains greater than 0.015 up to the point of tensile instability. It is interesting to observe that similar tensile properties, measured in MT and LT specimens, can be achieved with different flow behaviour due to differences in work-hardening behaviour.

3.3. Effect of martensite strength on flow stress

The isotropic and anisotropic strains with applied stress of different phases and plane orientations are depicted in Fig. 3. Anisotropic lattice strains, tensile in character in planes oriented in the axial direction and compressive in character in planes oriented in the radial direction, increase linearly at low applied stress and thus are associated with elastic deformation of different phases. At higher applied stresses, a deviation from linearity is observed in most of the planes, which is evidence of the development of plastic strains. Isotropic strains become evident coinciding with transformation of austenite. While in {200}γ planes, isotropic strains increase in tension, isotropic strains in {220}γ tend to increase in compression with applied stress. Isotropic strain in {200}α' increases in tension to a lesser extent compared to {200}γ and barely changes in {211}α' as applied stress increases. These results are in agreement with common observations in mechanical induced transformation of austenite [24].

The stress calculated using elastic strain of specific lattice planes of austenite and martensite as a function of applied stress is depicted in Fig. 7b. The yield strengths of austenite $\sigma_Y\gamma$ and martensite $\sigma_Y\alpha$ are plotted in Fig. 7a. The strength of martensite, evaluated through the yield point, varies in the three microstructures, whereas austenite has a similar strength in all three conditions. The yield strength of martensite is 1150 MPa, 929 MPa and 740 MPa in LT, MT and HT specimens respectively. The strength of the martensite is reduced with the severity of the tempering due to a reduction of the dislocation density and carbon in solid solution.

In contrast, austenite dislocation density, grain size and solute content are not significantly affected during the applied heat treatments. There is a slight reduction of the yield strength of austenite as the severity of tempering increases; the austenite yield strength is 990 MPa, 890 MPa 870 MPa for LT, MT and HT specimens, respectively. These values are in good agreement with that estimated from Eq. (12). The decrease of the strength of austenite is attributed to partial recovery. It is worth noting that yield stress values of austenite, higher than typical for fully austenitic microstructures, can be a consequence of stress triaxiality induced by the constraints from the surrounding martensite [36].

Overall, the three heat treatments produced three distinct variations in strength ratio between martensite and austenite: the strength of martensite is higher than austenite (LT), austenite and martensite have similar strength (MT), and the strength of austenite is higher than martensite (HT).

The fraction of austenite with applied stress is shown in Fig. 7c. The differences in mechanical stability of austenite in the different microstructures can be attributed to the strength of martensite. Comparing the stress at the onset of decomposition and decomposition ratios of austenite in different microstructures, it is concluded that austenite surrounded by a stronger martensitic matrix (LT) is mechanically more stable than austenite surrounded by a weaker martensite (HT). If the strength of martensite is higher than or equal to that of the austenite, austenite begins to decompose after yielding (LT and MT) and the transformation is said to be strain-assisted. Moreover, the transformation accelerates when the martensite yields, suggesting that martensite prevents austenite from decomposition when martensite is still in the elastic deformation regime (LT).

If the strength of martensite is lower than that of austenite (HT), transformation of austenite occurs at stresses well below the austenite and martensite yield stress. The transformation is thus stress-assisted. The austenite (FCC) to martensite (BCC) transformation is accompanied by volume expansion, which causes deformation of the surroundings, i.e. primarily the martensite. In HT, low martensite strength facilitates the volume expansion associated to the onset of the transformation. Moreover, hydrostatic compressive stresses resulting from the martensite formation, as proposed by Allain et al. [34], are likely reduced with increasing tempering severity in HT. This explains the early onset of austenite to martensite transformation in HT. These results demonstrate that the strength of the surrounding phase is a critical factor in the stress level for the onset of transformation.

The work-hardening rate as a function of stress, commonly known as a Kocks-Mecking plot, is displayed in Fig. 7d. The anelastic pre-yield region, shadowed in grey in Fig. 7d, is characterized by a rapid decrease in the work-hardening rate with stress. An inflection is observed at the

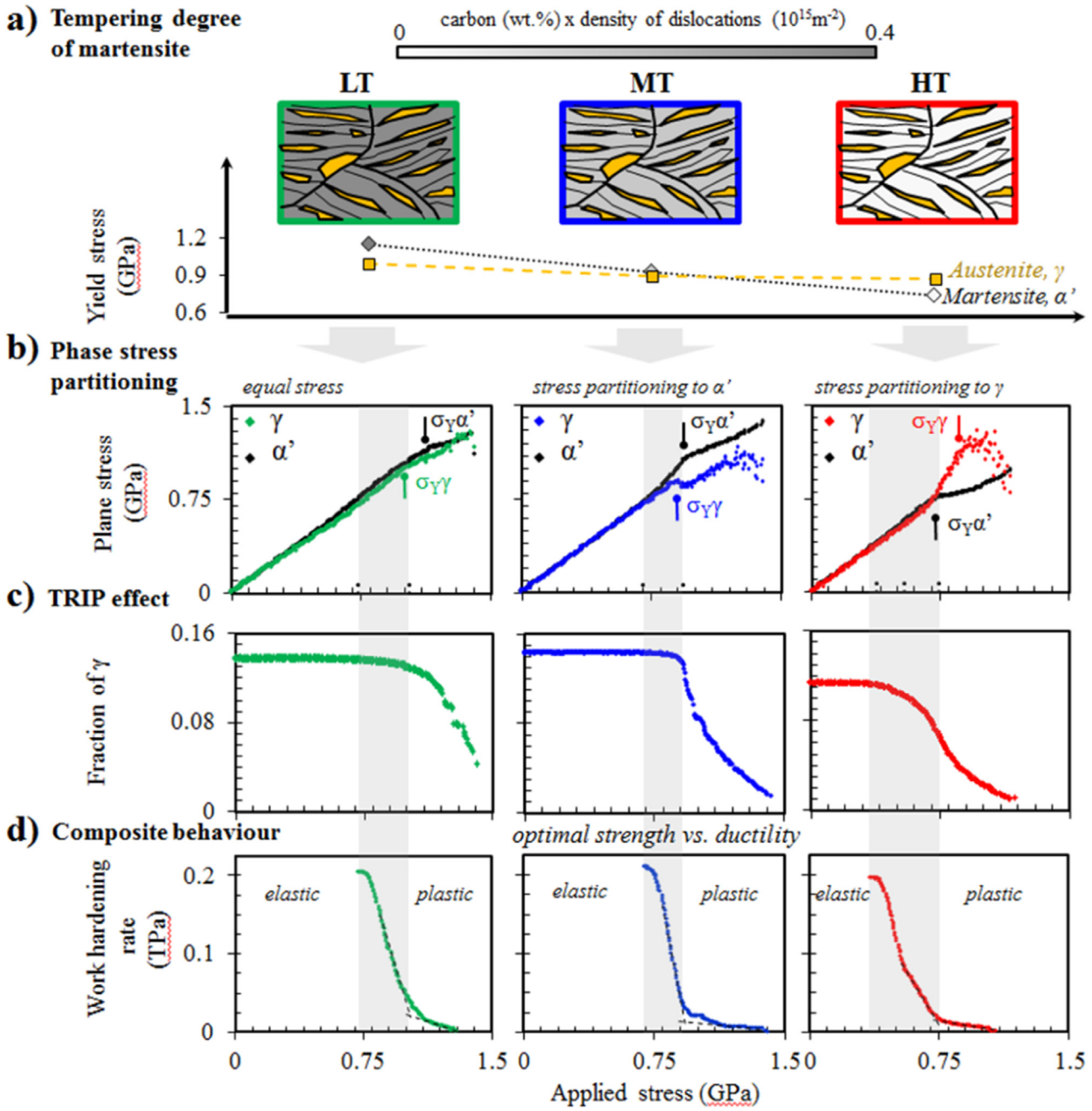

Fig. 7. Separation of the different factors influencing mechanical response of steels with different strength ratios between austenite, γ, and martensite, α', phases. (a) Schematic of the three different microstructures studied emphasizing the differences in strength of γ (yellow) and α' (grey). LT, MT and HT indicate low, medium and high degree of tempering, respectively. The grey scale is linked with the parameter carbon content multiplied by dislocation density in martensite and highlights the degree of martensite tempering [20]. (b) Plane stress calculations from {200} reflections of austenite and martensite indicating the development of stress partitioning between both phases during deformation. The yielding of each phase (σ_Y) is indicated with circular-head arrows. (c) Fraction of austenite with stress indicating the occurrence of the mechanically induced transformation also referred as TRIP effect. (d) Work-hardening rate with stress, showing the purely elastic, anelastic (delimited by vertical grey bands) and plastic region of the composite material [29]. The intersection of the dashed lines delineates the yield stress.

end of the anelastic region, marking the transition to plastic deformation [37]. For multiphase materials in the present study, the transition is gradual, indicating continuous yielding. The transition to the plastic regime is mainly controlled by the martensite yielding in all microstructures, as it is the dominant phase. The observed work-hardening behaviour of the steel beyond the yield point is affected by mechanically-induced formation of martensite and work-hardening of individual phases through dislocation movement and multiplication. These mechanisms depend on strain/stress partitioning between the different phases.

Fig. 8 shows the evolution of average carbon content in austenite with austenite fraction. In the LT specimen, the average carbon content continuously increases when the fraction of austenite is reduced, indicating that the carbon is not homogeneous across the austenite. Low carbon content austenite is softer and has low stability [38]. Hence, it yields and decomposes first. The remaining untransformed austenite is stronger and more stable. The carbon content in austenite does not vary significantly in MT and LT specimens with decreasing fractions of austenite. This indicates that carbon distribution is homogeneous in austenite and thus the contribution of carbon to the strength and

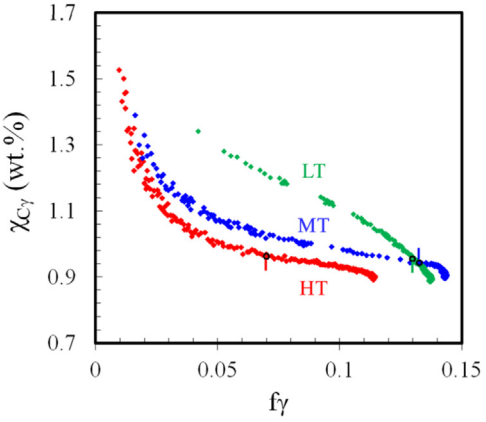

Fig. 8. Evolution of average carbon content in austenite $\chi_{C\gamma}$ with austenite fraction during tensile testing. The fraction of austenite and its correspondent carbon content at yield point is indicated in every case with an arrow. The estimated error in $\chi_{C\gamma}$ is around 0.02.

stability of austenite does not vary as the austenite transformation progresses.

The effect of strength ratio between austenite and martensite phases on the mechanical response is further discussed next:

1. In the LT microstructure as shown in Fig. 7a, martensite is the least tempered among all microstructures and the yield strength of martensite is initially higher than that of austenite. When austenite yields, martensite is still in the elastic regime and does not contribute to the work hardening. Moreover, austenite transformation is prevented before the yielding of martensite due to the effect of strong martensite as previously discussed. Hence, the strain is partitioned to austenite, which rapidly work hardens and compensates for the initial stress difference between austenite and martensite (approx. 100 MPa). The increase of carbon content in austenite with applied stress (see Fig. 8) also contributes to reduced strength difference between phases. Once martensite yields, the difference in the work hardening capacity between austenite and martensite [38] makes the stress more equally partitioned in both phases. All these factors explain the low stress partitioning between austenite and martensite in the LT specimen, as shown Fig. 7b. The increase of carbon concentration in austenite with austenite transformation and the low plastic deformation capacity of martensite slow down the further transformation of austenite resulting in low decomposition rates as depicted in Fig. 7c. This limits the contribution of austenite decomposition to the uniform elongation and work-hardening of the material, moderating the ductility of the material despite the high strengths that are achieved. This is clearly seen in the evolution of instantaneous work-hardening rate with true strain of LT specimen in Fig. 6.
2. Similar strength of martensite and austenite (MT microstructure in Fig. 7a) results in higher ductility and high strength levels of the steel. The decrease of dislocation density and carbon in solid solution decreases the flow strength of martensite, i.e. its capacity to plastically deform and accommodate volume expansion due to austenite transformation increases. Austenite severely destabilizes when martensite yields and high austenite decomposition rates are maintained during the plastic flow (Fig. 7c); thus, there is a larger impact of the austenite mechanically-induced transformation on the uniform plastic elongation compared to the LT condition. The decomposition rate at high stresses decreases, which is likely due to strengthening of martensite, increase of average carbon concentration in austenite, and decrease of the austenite grain size. Moreover, hard freshly-formed martensite from austenite decomposition further contributes to the strengthening and work-hardening of the steel. The high austenite transformation rates at the beginning of the plastic deformation and the fact that freshly formed martensite is stronger and has high work hardening rate [38], might cause stress to preferentially partition to martensite as shown in Fig. 7b. It is worth noting that for martensite, the peak broadening is more severe in the MT condition (see Fig. 4), which suggests higher work-hardening of the martensite compared to LT or HT conditions. Moreover, the carbon in austenite remains unaltered in this stress interval, and thus it is not affecting the strength of austenite as in LT condition. The stress difference between austenite and martensite phases progressively reduces coinciding with a decreasing in the austenite transformation rate.
3. An increase of the severity of tempering (HT microstructure in Fig. 7a) further reduces the dislocation density and carbon content of martensite. In this condition, the strength of austenite exceeds that of martensite. Austenite rapidly decomposes before macroscopic yielding of the microstructure. In Fig. 7c for the HT microstructure, half of the austenite is already transformed at the onset of plasticity making the contribution of austenite transformation to uniform strain less effective than the other conditions. However, the highly tempered martensite with low yield strength in HT specimen contributes to more uniform elongation and work-hardening compared to that obtained when the strength of phases is more alike (MT microstructure). The work-hardening of austenite and mechanically induced martensite formed at early stages enhance uniform elongation. Moreover, stress is strongly partitioned to austenite as depicted in Fig. 7b, even more than the stress partitioned to martensite in the MT condition. The internal stress generated by the plastic misfit strain from transformation contributes to the increased work-hardening, which delays the onset of plastic flow instabilities [1]. Nevertheless, more severely tempered soft martensite leads to low strength.

4. Conclusions

In-situ high-energy synchrotron X-ray diffraction allowed monitoring of the behaviour of individual phases during application of stress to steels consisting of martensite/austenite microstructures in which the strength ratio between martensite and austenite was varied by three different levels of tempering: low tempering, medium tempering and high tempering. Several novel findings related to deformation of multiphase steels were extracted from this study:

1) The strength ratio between the martensite and austenite governs the mechanical performance of the steel by controlling the stress partitioning between the microconstituents and regulating the decomposition of retained austenite with deformation. The work-hardening of the individual microconstituents and the decomposition rate of the retained austenite dictates the work-hardening of multiphase steels.
2) The austenite yield strength may become comparable and higher than the martensite yield strength with increasing tempering. The stress partitions to the austenite with increasing strain in this condition, even more than the stress partitions to martensite for the medium tempering condition.
3) The extent of work hardening in the martensite is greater in the medium tempering condition than the low tempering condition, which affects the stress partitioning and results in the most optimal combination of strength and ductility of the three evaluated conditions.

Acknowledgments

The authors want to acknowledge Alfonso Navarro, Bij-Na Kim, Parisa Eftekharimilani and Andrea Bernasconi for their help and support during the performing of the experimental work at ESRF facilities

and to Jilt Sietsma for the wise advices in the present work. The research leading to these results has received funding from the European Research Council under the European Union's Seventh Framework Programme (FP/2007-2013)/ERC Grant Agreement no. [306292].

Data availability

The raw and processed data required to reproduce the findings of this research study are available to download from the Supplementary material.

Appendix A. Supporting information

Supplementary data associated with this article can be found in the online version at doi:10.1016/j.msea.2018.12.096.

References

[1] Y. Tomota, H. Tokuda, Y. Adachi, M. Wakita, N. Minakawa, A. Moriai, Y. Morii, Tensile behavior of TRIP-aided multi-phase steels studied by in situ neutron diffraction, Acta Mater. 52 (2004) 5737–5745.
[2] F. HajyAkbary, J. Sietsma, G. Miyamoto, N. Kamikawa, R.H. Petrov, T. Furuhara, M.J. Santofimia, Analysis of the mechanical behavior of a 0.3C-1.6Si-3.5Mn (wt%) quenching and partitioning steel, Mater. Sci. Eng. A 677 (2016) 505–514.
[3] M. Koyama, Z. Zhang, M. Wang, D. Ponge, D. Raabe, K. Tsuzaki, H. Noguchi, C.C. Tasan, Bone-like crack resistance in hierarchical metastable nanolaminate steels, Science 355 (2017) 1055–1057.
[4] D.K. Matlock, J.G. Speer, Third generation of AHSS: microstructure design concepts, in: A. Steels, S. Haldar, Suwas, D. Bhattacharjee (Eds.), Microstructure and Texture, Springer, London, 2009, pp. 185–205.
[5] E.J. Seo, L. Cho, Y. Estrin, B.C. De Cooman, Microstructure-mechanical properties relationships for quenching and partitioning (Q&P) processed steel, Acta Mater. 113 (2016) 124–139.
[6] S.S. Sohn, H. Song, M.C. Jo, T. Song, H.S. Kim, S. Lee, Novel 1.5 GPa-strength with 50%-ductility by transformation-induced plasticity of non-recrystallized austenite in duplex steels, Sci. Rep. 7 (2017).
[7] J.G. Speer, E. De Moor, A.J. Clarke, Critical assessment 7: quenching and partitioning, Mater. Sci. Technol. 31 (2015) 3–9.
[8] B.C. De Cooman, Structure–properties relationship in TRIP steels containing carbide-free bainite, Curr. Opin. Solid State Mater. Sci. 8 (2004) 285–303.
[9] B.L. Ennis, E. Jimenez-Melero, E.H. Atzema, M. Krugla, M.A. Azeem, D. Rowley, D. Daisenberger, D.N. Hanlon, P.D. Lee, Metastable austenite driven work-hardening behaviour in a TRIP-assisted dual phase steel, Int. J. Plast. 88 (2017).
[10] R.J. Moat, S.Y. Zhang, J. Kelleher, A.F. Mark, T. Mori, P.J. Withers, Work hardening induced by martensite during transformation-induced plasticity in plain carbon steel, Acta Mater. 60 (2012) 6931–6939.
[11] I. de Diego-Calderón, M.J. Santofimia, J.M. Molina-Aldareguia, M.A. Monclús, I. Sabirov, Deformation behavior of a high strength multiphase steel at macro- and micro-scales, Mater. Sci. Eng. A 611 (2014) 201–211.
[12] D. De Knijf, C. Föjer, L.A.I. Kestens, R. Petrov, Factors influencing the austenite stability during tensile testing of Quenching and Partitioning steel determined via in-situ electron backscatter diffraction, Mater. Sci. Eng. A 638 (2015) 219–227.
[13] R.D.K. Misra, V.S.A. Challa, P.K.C. Venkatsurya, Y.F. Shen, M.C. Somani, L.P. Karjalainen, Interplay between grain structure, deformation mechanisms and austenite stability in phase-reversion-induced nanograined/ultrafine-grained austenitic ferrous alloy, Acta Mater. 84 (2015) 339–348.
[14] X.C. Xiong, B. Chen, M.X. Huang, J.F. Wang, L. Wang, The effect of morphology on the stability of retained austenite in a quenched and partitioned steel, Scr. Mater. 68 (2013) 321–324.
[15] B. Fultz, J.W. Morris, The mechanical stability of precipitated austenite in 9Ni steel, Metall. Trans. A 16 (1985) 2251–2256.
[16] I. Karaman, M. Balzer, H. Sehitoglu, H.J. Maier, Stress-state effects on the stress-induced martensitic transformation of carburized 4320 steels, Metall. Mater. Trans. A 29 (1998) 427–437.
[17] P.J. Jacques, F. Delannay, J. Ladrière, On the influence of interactions between phases on the mechanical stability of retained austenite in transformation-induced plasticity multiphase steels, Metall. Mater. Trans. A 32 (2001) 2759–2768.
[18] C.Y. Wang, J. Shi, W.Q. Cao, H. Dong, Characterization of microstructure obtained by quenching and partitioning process in low alloy martensitic steel, Mater. Sci. Eng. A 527 (2010) 3442–3449.
[19] D. De Knijf, R. Petrov, C. Föjer, L.A.I. Kestens, Effect of fresh martensite on the stability of retained austenite in quenching and partitioning steel, Mater. Sci. Eng. A 615 (2014) 107–115.
[20] W.S. Li, H.Y. Gao, H. Nakashima, S. Hata, W.H. Tian, In-situ study of the deformation-induced rotation and transformation of retained austenite in a low-carbon steel treated by the quenching and partitioning process, Mater. Sci. Eng. A 649 (2016) 417–425.
[21] K.O. Findley, J. Hidalgo, R.M. Huizenga, M.J. Santofimia, Controlling the work hardening of martensite to increase the strength/ductility balance in quenched and partitioned steels, Mater. Des. 117 (2017) 248–256.
[22] R. Blondé, E. Jimenez-Melero, L. Zhao, J.P. Wright, E. Brück, S. van der Zwaag, N.H. van Dijk, Mechanical stability of individual austenite grains in TRIP steel studied by synchrotron X-ray diffraction during tensile loading, Mater. Sci. Eng. A 618 (2014) 280–287.
[23] E. Jimenez-Melero, N.H. van Dijk, L. Zhao, J. Sietsma, J.P. Wright, S. van der Zwaag, In situ synchrotron study on the interplay between martensite formation, texture evolution and load partitioning in low-alloyed TRIP steels, Mater. Sci. Eng. A 528 (2011) 6407–6416.
[24] J.H. Jung, H.S. Kim, B.C. DeCooman, In-situ synchrotron XRD analysis of the effect of static strain aging on the elasto-plastic transition in CMnSi TRIP steel, Steel Res. Int. 80 (2009) 515–520.
[25] J. Hidalgo, K.O. Findley, M.J. Santofimia, Thermal and mechanical stability of retained austenite surrounded by martensite with different degrees of tempering, Mater. Sci. Eng. A 690 (2017) 337–347.
[26] A.P. Hammersley, FIT2D: a multi-purpose data reduction, analysis and visualization program, J. Appl. Crystallogr. 49 (2016) 646–652.
[27] R. Blondé, E. Jimenez-Melero, L. Zhao, J.P. Wright, E. Brück, S. Van Der Zwaag, N.H. Van Dijk, High-energy X-ray diffraction study on the temperature-dependent mechanical stability of retained austenite in low-alloyed TRIP steels, Acta Mater. 60 (2012) 565–577.
[28] ASTM International, Standard Practice for X-Ray Determination of Retained Austenite in Steel with Near Random Crystallographic Orientation. West Conshohocken, PA, 2013.
[29] N.H. Van Dijk, A.M. Butt, L. Zhao, J. Sietsma, S.E. Offerman, J.P. Wright, S. Van Der Zwaag, Thermal stability of retained austenite in TRIP steels studied by synchrotron X-ray diffraction during cooling, Acta Mater. 53 (2005) 5439–5447.
[30] M. Villa, F. Niessen, M.A.J. Somers, In situ investigation of the evolution of lattice strain and stresses in austenite and martensite during quenching and tempering of steel, Metall. Trans. A 49 (2018) 28–40.
[31] F.M. McGuire, Stainless Steels for Design Engineers, ASM International, Materials Park, Ohio, 2008.
[32] B. Hutchinson, J. Hagström, O. Karlsson, D. Lindell, M. Tornberg, F. Lindberg, M. Thuvander, Microstructures and hardness of as-quenched martensites (0.1-0.5%C), Acta Mater. 59 (2011) 5845–5858.
[33] N. Ridley, H. Stuart, Lattice parameter anomalies at the curie point of pure iron, J. Phys. D: Appl. Phys. 1 (1968) 1291–1295.
[34] S.Y.P. Allain, S. Gaudez, G. Geandier, J.-C. Hell, M. Gouné, F. Danoix, M. Soler, S. Aoued, A. Poulon-Quintin, Internal stresses and carbon enrichment in austenite of Quenching and Partitioning steels from high energy X-ray diffraction experiments, Mater. Sci. Eng. A 710 (2018) 245–250.
[35] Y.D. Wang, R. Lin Peng, X.L. Wang, R.L. McGreevy, Grain-orientation-dependent residual stress and the effect of annealing in cold-rolled stainless steel, Acta Mater. 50 (2002) 1717–1734.
[36] X. Lei, C. Li, X. Shi, X. Xu, Y. Wei, Notch strengthening or weakening governed by transition of shear failure to normal mode fracture, Sci. Rep. 5 (2015).
[37] P. van Liempt, J. Sietsma, A physically based yield criterion I. determination of the yield stress based on analysis of pre-yield dislocation behaviour, Mater. Sci. Eng. A 662 (2016) 80–87.
[38] X. Hu, K.S. Choi, X. Sun, Y. Ren, Y. Wang, Determining individual phase flow properties in a quench and partitioning steel with in situ high-energy x-ray diffraction and multiphase elasto-plastic self-consistent method, Metall. Mater. Trans. A 47 (2016) 5733–5749.